



# Exploring the synergistic role of electron-rich Pd and electron-deficient Ni in promoting electrocatalytic hydrodechlorination

Junjing Li<sup>a,\*</sup>, Kaizhou Kong<sup>a</sup>, Shumin Ma<sup>a</sup>, Jing Ding<sup>b</sup>, Liang Wang<sup>a,c,\*</sup>, John C. Crittenden<sup>d</sup>

<sup>a</sup> School of Environmental Science and Engineering, Tiangong University, State Key Laboratory of Separation Membranes and Membrane Processes, Binshui West Road 399, Xiqing District, Tianjin 300387, PR China

<sup>b</sup> State Key Laboratory of Urban Water Resource and Environment, Harbin Institute of Technology, Harbin 150090, PR China

<sup>c</sup> Cangzhou Institute of Tiangong University, East side of No.13 Fengtai Park, High-tech District, Cangzhou 061019, PR China

<sup>d</sup> Georgia Institute of Technology, 828 West Peachtree Street, Atlanta, GA 30332, United States

## ARTICLE INFO

### Keywords:

Electrocatalytic hydrodechlorination

Catalysts

Synergistic catalysis

Palladium

Environmental remediation

## ABSTRACT

Pd has been widely used in electrocatalytic hydrodechlorination (EHDC) due to its excellent catalytic properties, but the expensive price limits its large-scale application. To address the above issues, Pd/NiFeP-Ti<sub>3</sub>C<sub>2</sub>T<sub>x</sub>/NF electrodes with excellent EHDC capability are prepared by introducing the electron-rich Pd and the electron-deficient Ni. The synergistic role of electron-rich Pd and electron-deficient Ni lowers the energy barrier for active hydrogen (H\*) generation by water splitting, thus endowing Pd/NiFeP-Ti<sub>3</sub>C<sub>2</sub>T<sub>x</sub>/NF electrodes excellent ability to generate H\*. H\* has the lowest migration barrier between Pd and Ni, thus Pd and Ni produce large amounts of H\* that can freely migrate to attack adsorbed chlorinated pollutants. Compared to other catalysts, Pd/NiFeP-Ti<sub>3</sub>C<sub>2</sub>T<sub>x</sub>/NF electrode has the highest mass activity and can remove various emerging chlorinated pharmaceuticals and personal care products (PPCPs). This is a novel strategy to prepare low-cost electrodes with excellent performance to facilitate the practical application of EHDC technology.

## 1. Introduction

Chlorinated pharmaceuticals and personal care products (PPCPs) have larger molecular weights and higher levels of hydrophobicity due to the presence of elemental chlorine, and they are more bio-accumulative, persistent and toxic than other PPCPs that do not contain chlorine [1,2]. Electrocatalytic hydrodechlorination (EHDC) reaction produces active hydrogen (H\*) on the cathode surface by easily transferring electrons to the H<sub>2</sub>O molecule. H\* can attack and cleave the C–Cl bond, thus reducing the toxicity and chemical stability of pollutants [3,4]. H\* is the only active substance that reduces a wide variety of chlorinated pollutants. Therefore, the generation and utilization of H\* are very important in the EHDC process. Pd metal is considered as the most promising catalyst for EHDC reactions due to its suitable adsorption energy and good performance in H\* generation and storage [5]. However, the high cost, ease of aggregation and deactivation problems of the Pd have seriously hindered its large-scale application [6]. It is desirable to seek a feasible solution to improve the intrinsic activities of Pd and simultaneously reduce the amount of Pd for EHDC reactions.

Numerous effective strategies are commonly used to prepare high-

performance catalysts, for example: (1) Optimization of the electronic structure of the catalyst [7,8]; (2) Preparation of 3D-structured catalysts to expose more active sites [9]; and, (3) Improvement of catalyst conductivity to accelerate electron transfer [10,11]. Transition metal phosphides (TMPs) are ideal electrocatalysts for water splitting owing to the slightly higher electronegativity of phosphorus compared with most of the transition metal elements [12,13]. Among them, Ni-Fe phosphide (NiFeP) has been proved as the highly efficient electrocatalyst since the significant synergism between Ni and Fe is conducive to the occurrence of overall water electrolysis [14]. However, the low conductivity and poor stability limit the application of TMPs [15]. Fortunately, composite structures provide an effective strategy to solve the above problems. Ti<sub>3</sub>C<sub>2</sub>T<sub>x</sub> (MXene) is a new family of 2D materials with an abundance of active sites and excellent electrical conductivity [16]. It is believed that the combination of NiFeP and Ti<sub>3</sub>C<sub>2</sub>T<sub>x</sub> materials can obtain an optimized electronic structure and promote the splitting of water to produce H\*, which can enhance the EHDC performance of catalysts.

The abundant heterogeneous interfaces between different functional components can fully expose the active sites and adjust the electronic structure of the catalysts, thus increasing the intrinsic catalytic activity

\* Correspondence to: School of Environmental Science and Engineering, Tiangong University, Binshui West Road 399, Xiqing District, Tianjin 300387, PR China.  
E-mail addresses: [junjingli85@163.com](mailto:junjingli85@163.com) (J. Li), [mashi7822@163.com](mailto:mashi7822@163.com) (L. Wang).

<https://doi.org/10.1016/j.apcatb.2024.124245>

Received 30 March 2024; Received in revised form 14 May 2024; Accepted 26 May 2024

Available online 27 May 2024

0926-3373/© 2024 Published by Elsevier B.V.

of water splitting [17]. In this work, Pd is combined with NiFeP-Ti<sub>3</sub>C<sub>2</sub>T<sub>x</sub> with different properties to form a Pd/NiFeP-Ti<sub>3</sub>C<sub>2</sub>T<sub>x</sub> heterojunction catalyst using nickel foam (NF) as a substrate. Structural and morphological characterization demonstrates Pd particles form uniformly sized clusters on NiFeP-Ti<sub>3</sub>C<sub>2</sub>T<sub>x</sub> and electron transfer occurs between Pd and NiFeP-Ti<sub>3</sub>C<sub>2</sub>T<sub>x</sub>. Density functional theory (DFT) and experiments demonstrate the mechanism of electron transfer and the synergistic role of electron-rich Pd and electron-deficient Ni for the EHDC process. Superior structure gives the electrode excellent EHDC efficiency, stability and the highest mass activity.

## 2. Materials and methods

### 2.1. Materials

Platinum sheet and nickel foam (NF) were purchased from Heze Tianyu Technology Development Co., Ltd. The multilayer Ti<sub>3</sub>C<sub>2</sub>T<sub>x</sub> MXene solution was purchased from Suzhou Beike Nano Technology Co., Ltd. Nickel chloride hexahydrate (NiCl<sub>2</sub>·6H<sub>2</sub>O), ferric nitrate nonahydrate (Fe(NO<sub>3</sub>)<sub>3</sub>·9H<sub>2</sub>O), thiourea, and ammonium fluoride (NH<sub>4</sub>F) were obtained from Shanghai Macklin Biochemical Co., Ltd.

### 2.2. Electrode preparation

Pd/NiFeP-Ti<sub>3</sub>C<sub>2</sub>T<sub>x</sub>/NF electrodes with excellent electronic structure were prepared by hydrothermal, phosphating calcination and electrochemical methods. The detailed process of the electrode preparation was provided in Text S1 and Fig. 1a.

### 2.3. Theoretical calculation

All DFT calculations were implemented by the Vienna Ab-initio Simulation Package (VASP) software based on density generalization. The solvent effects were eliminated by the solvation program VASP-sol. See Text S2 for details of DFT calculations.

### 2.4. Electrode characterization

The surface morphology and elemental distribution of the electrodes were observed using a scanning electron microscope (SEM, FEI Quanta FEG 250, USA) equipped with energy dispersive X-ray spectroscopy (EDS). The electrode morphology, size, and the lattice fringes of Pd nanoparticles on the electrodes were observed by transmission electron microscopy (TEM, JEOL JEM 2100Plus, Japan). X-ray diffraction (XRD,

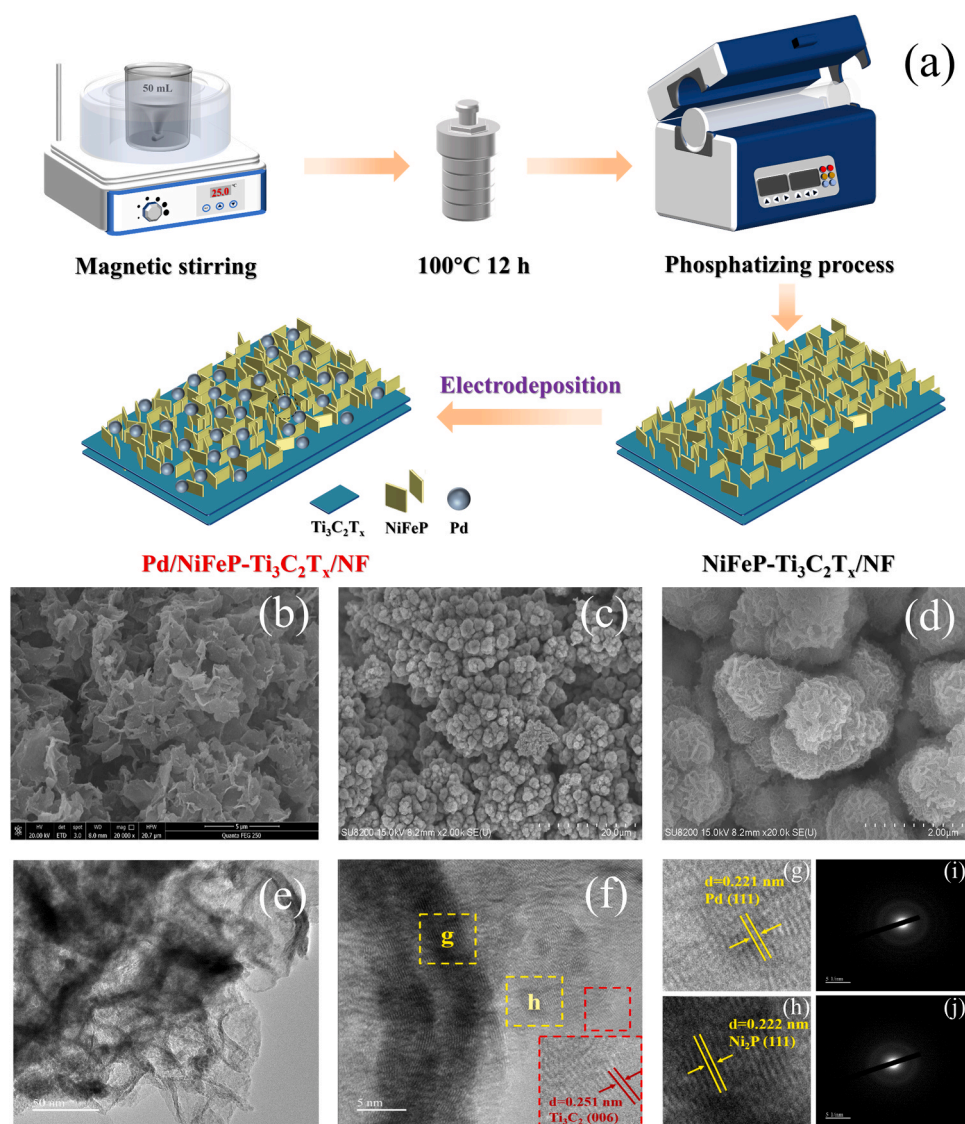


**Fig. 1.** (a) Schematic diagram of Pd/NiFeP-Ti<sub>3</sub>C<sub>2</sub>T<sub>x</sub>/NF electrode preparation, SEM images of NiFeP-Ti<sub>3</sub>C<sub>2</sub>T<sub>x</sub>/NF electrode (b) 20,000 $\times$ , SEM images of Pd/NiFeP-Ti<sub>3</sub>C<sub>2</sub>T<sub>x</sub>/NF electrode at different magnifications (c) 2,000 $\times$ , (d) 20,000 $\times$ , (e) TEM images of Pd/NiFeP-Ti<sub>3</sub>C<sub>2</sub>T<sub>x</sub>/NF electrode, (f-h) HRTEM, (i, j) SAED.

Bruker D8 Advance, Germany) was used to analyze the physical phase composition of the electrodes. The electronic states of the component elements of the electrode surface were studied using X-ray photoelectron spectroscopy (XPS, Thermo Fisher NEXSA, USA). Detailed information on the coordination environment of Pd on the Pd/NiFeP-Ti<sub>3</sub>C<sub>2</sub>T<sub>x</sub>/NF electrode was obtained by X-ray adsorption spectra (XAS) testing and analysis (Text S3). Detailed information on electrochemical testing was described in Text S4.

## 2.5. Electrocatalytic hydrodechlorination experiments

Details of the EHDC experiments were presented in Text S5. The concentration profiles of chlorinated PPCPs during EHDC were obtained by determining the peak areas using high performance liquid chromatography (HPLC, Shimadzu LC-20AT, Japan). The liquid chromatographic procedures for different chlorinated PPCPs were described in Text S6.

## 3. Results and discussion

### 3.1. Characterization of the morphology and structure

The surface morphology and composition of the electrodes were observed by SEM. NiFeP and Ti<sub>3</sub>C<sub>2</sub>T<sub>x</sub> form a fully exposed vertically interleaved array, and NiFeP can be used as a spacer layer at the same time, which avoids the aggregation of the ultrathin Ti<sub>3</sub>C<sub>2</sub>T<sub>x</sub> layer (Fig. 1b). This ultrathin porous structure with high specific surface area provides more exposed active sites for electrode reactions. The Pd/NiFeP-Ti<sub>3</sub>C<sub>2</sub>T<sub>x</sub>/NF electrode shows a self-supported electrode with a three-dimensional morphology. Uniformly sized cauliflower-like Pd clusters are grown on NiFeP-Ti<sub>3</sub>C<sub>2</sub>T<sub>x</sub>, which will greatly utilize the activity of the catalytic metal Pd thereby improving the electrocatalytic performance (Fig. 1c-d). The EDS shows the relatively uniform distribution of Pd particles, and the elemental composition of the Pd/NiFeP-Ti<sub>3</sub>C<sub>2</sub>T<sub>x</sub>/NF electrode (Figure S4). SEM analyses of Pd/Ti<sub>3</sub>C<sub>2</sub>T<sub>x</sub>/NF and Pd/NiFeP/NF electrodes are discussed in Text S7.

The degree of homogeneous dispersion of Pd on the surfaces of electrodes are observed by TEM. The Pd/NiFeP/NF electrode shows an irregular flower-like structure, but the Pd nanoparticles on the electrode surface are not uniformly dispersed and are in very small quantities, which is due to the aggregation phenomenon of Pd (Figure S5a). The Pd/Ti<sub>3</sub>C<sub>2</sub>T<sub>x</sub>/NF electrode exhibits an ultrathin nanosheet structure, and although the Pd nanoparticles are dispersed on the surface, the Ti<sub>3</sub>C<sub>2</sub>T<sub>x</sub> nanosheets are still aggregated (Figure S5b). This makes it difficult to ensure the uniform dispersion of Pd nanoparticles. Clearly, NiFeP nanosheets are firmly rooted in the ultrathin Ti<sub>3</sub>C<sub>2</sub>T<sub>x</sub>, which presents a rougher surface. Pd nanoparticles are uniformly distributed on the NiFeP-Ti<sub>3</sub>C<sub>2</sub>T<sub>x</sub> composite structure (Fig. 1e). The results show that NiFeP-Ti<sub>3</sub>C<sub>2</sub>T<sub>x</sub> interlayer solves the problem of Pd nanoparticles are prone to agglomeration to a certain extent. High-resolution transmission electron microscope (HRTEM) and selected area electron diffraction (SAED) images show clear lattice fringes of Ti<sub>3</sub>C<sub>2</sub>, Pd and Ni<sub>2</sub>P (Fig. 1f-j). Lattice spacings of 0.251 nm, 0.221 nm, and 0.222 nm correspond to the Ti<sub>3</sub>C<sub>2</sub> (006) plane, Pd (111) plane, and Ni<sub>2</sub>P (111) plane, respectively. The TEM-mapping images of the Pd/NiFeP-Ti<sub>3</sub>C<sub>2</sub>T<sub>x</sub>/NF electrode show the uniform distribution of the elements Ni, Fe, Pd, C, P, and Ti, further indicating the successful loading of Pd on the NiFeP-Ti<sub>3</sub>C<sub>2</sub>T<sub>x</sub> structure (Figure S6).

The crystal structure of the electrode was determined by XRD (Figure S7). The diffraction peaks in the XRD images of the three electrodes at 44.326°, 51.715°, and 76.373° correspond to the (111), (200), and (220) crystal planes of Ni (JCPDS No. 04-0850), respectively. The XRD images of the Pd/NiFeP/NF and Pd/NiFeP-Ti<sub>3</sub>C<sub>2</sub>T<sub>x</sub>/NF electrodes show diffraction peaks similar to those of Ni<sub>2</sub>P at 40.449°, 44.739°, 47.148°, 54.599°, 55.201°, 73.039°, and 88.919°, which correspond to (111), (201), (210), (300), (211), (311), and (321) crystal planes of the

hexagonal Ni<sub>2</sub>P (JCPDS No. 03-0953), respectively. This confirms the conversion of Ni-Fe precursor to NiFeP after in situ phosphating of the electrode. However, the phosphide diffraction peaks of Fe are not detected in XRD, implying that Fe atoms may be doped into the lattice sites of Ni<sub>2</sub>P, which can enhance the activity of the metal and improve the catalytic efficiency. The diffraction peak intensity of the Pd (111) crystal plane is much stronger than that of the other crystal planes, which is consistent with the results of HRTEM analysis. Additionally, the diffraction peaks from Ti<sub>3</sub>C<sub>2</sub>T<sub>x</sub> are not visible due to the extremely strong diffraction peaks of NF [18].

### 3.2. Elemental composition and coordination environment of the electrodes

The elemental composition and chemical valence states of the electrodes were analyzed by XPS. The peaks at 284.79 eV, 286.80 eV, 288.80 eV, and 281.50 eV correspond to the C-C, C-O-C, O-C=O, and Ti-C bonds, respectively (Figure S8a) [19]. The O 1s orbital exhibits an isolated peak at a binding energy of 531.15 eV, corresponding to the P-O bond (Figure S8b) [20].

To investigate the heterojunction effect formed between NiFeP-Ti<sub>3</sub>C<sub>2</sub>T<sub>x</sub> and Pd, the binding energy shifts of Ni 2p orbitals of Pd/NiFeP-Ti<sub>3</sub>C<sub>2</sub>T<sub>x</sub>/NF are shown in Fig. 2a. The peaks with binding energies at 855.58 eV and 873.18 eV are attributed to the Ni<sup>2+</sup> 2p<sub>3/2</sub> and Ni<sup>2+</sup> 2p<sub>1/2</sub> orbitals, respectively. The peaks with binding energies at 860.48 eV and 878.48 eV correspond to the satellite peaks of the Ni<sup>2+</sup> orbitals. Meanwhile, the binding energies are located at a pair of peaks 857.28 eV and 875.28 eV corresponding to the Ni<sup>3+</sup> 2p<sub>3/2</sub> and Ni<sup>3+</sup> 2p<sub>1/2</sub> orbitals, respectively. While the last pair of peaks with binding energies at 862.38 eV and 880.58 eV are attributed to the satellite peaks of the Ni<sup>3+</sup> orbitals [21]. Significantly, the binding energies of all peaks of the Ni 2p orbitals in the Pd/NiFeP-Ti<sub>3</sub>C<sub>2</sub>T<sub>x</sub>/NF electrode are increased compared to those reported in the literature, suggesting that the number of charges around the Ni element is reduced. Consequently, Ni<sup>2+</sup> will be oxidized to produce more highly valent Ni<sup>3+</sup>. Yang's groundbreaking research proves 3d transition metal-based electrocatalysts with a surface cation e<sub>g</sub> orbital occupancy approach unity [22]. However, e<sub>g</sub> occupancy is too low or too high (0 or 2, respectively), the binding of the electrocatalyst to oxygen will be too weak or too strong, respectively, resulting in poor water splitting performance. Compared with the t<sub>2g</sub><sup>6</sup>e<sub>g</sub><sup>2</sup> electronic configuration for Ni<sup>2+</sup>, Ni<sup>3+</sup> active sites in distorted possess a near-unity occupancy for the e<sub>g</sub> orbital (t<sub>2g</sub><sup>6</sup>e<sub>g</sub><sup>1</sup>) (Figure S9), which is ideal for efficient water splitting [23]. The Fe 2p and Pd 3d peaks of the Pd/NiFeP-Ti<sub>3</sub>C<sub>2</sub>T<sub>x</sub>/NF electrode are also analyzed (See Text S8 for details). The results show the electron transfer of Ni and Fe elements to Pd element has occurred.

XAS measurement is used to further probe the detailed coordination environment information of elemental Pd in the Pd/NiFeP-Ti<sub>3</sub>C<sub>2</sub>T<sub>x</sub>/NF electrode. The fine structure information of the Pd element in the Pd/NiFeP-Ti<sub>3</sub>C<sub>2</sub>T<sub>x</sub>/NF electrode is obtained by X-ray absorption near edge structure (XANES) spectrum. The valence state of Pd in the Pd/NiFeP-Ti<sub>3</sub>C<sub>2</sub>T<sub>x</sub>/NF electrode is predominantly zero-valent, and the contribution of the oxidized state of Pd to the signal is almost negligible (Figure S11). Subsequently the quantitative coordination environments of the Pd/NiFeP-Ti<sub>3</sub>C<sub>2</sub>T<sub>x</sub>/NF electrode and the Pd/NF electrode are analyzed by the extended absorption fine structure (EXAFS) spectrum. The EXAFs of R space indicates that the major peak of the Pd/NiFeP-Ti<sub>3</sub>C<sub>2</sub>T<sub>x</sub>/NF electrode is located at 2.73 Å, which suggests that the coordination environment of the Pd element in the Pd/NiFeP-Ti<sub>3</sub>C<sub>2</sub>T<sub>x</sub>/NF electrode is mainly a Pd-Pd bond (Fig. 2c). The data on XANES and EXAFs for the Pd/NF electrode are shown in Figure S12 and Table S1. The coordination numbers of Pd-Pd shell and Pd-O shell in the Pd/NiFeP-Ti<sub>3</sub>C<sub>2</sub>T<sub>x</sub>/NF electrode are 5.4 and 0.4, respectively, which are smaller than those of 6.8 and 1.5 in the Pd/NF electrode. Notably, the Pd element in the Pd/NiFeP-Ti<sub>3</sub>C<sub>2</sub>T<sub>x</sub>/NF electrode appears as a Pd-Ni shell with a bond length of about 2.62 Å and a coordination number of 1.6,



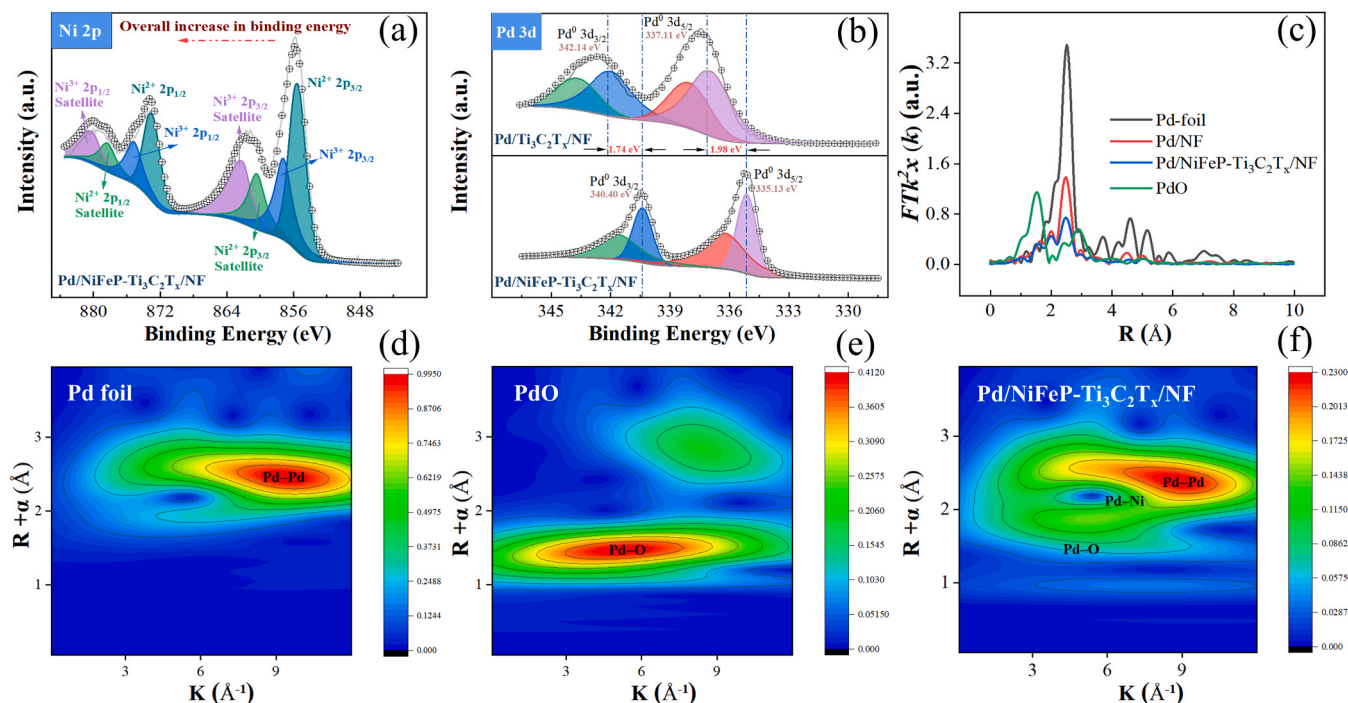


**Fig. 2.** (a) XPS of the Ni 2p orbitals of Pd/NiFeP-Ti<sub>3</sub>C<sub>2</sub>T<sub>x</sub>/NF electrode, (b) Pd 3d orbitals comparative spectra of Pd/Ti<sub>3</sub>C<sub>2</sub>T<sub>x</sub>/NF electrode and Pd/NiFeP-Ti<sub>3</sub>C<sub>2</sub>T<sub>x</sub>/NF electrode, (c) Fourier transformation of the Pd K-edge EXAFS spectra, Pd K-edge wavelet transform contour plots of (d) Pd foil, (e) PdO, and (f) Pd/NiFeP-Ti<sub>3</sub>C<sub>2</sub>T<sub>x</sub>/NF.

which does not appear in the Pd/NF electrode. This same result is found in the Pd K-edge wavelet transform contour plots of Fig. 2d-f and Figure S13, where at the maximum intensity of roughly  $6.6 \text{ \AA}^{-1}$ , the Pd/NiFeP-Ti<sub>3</sub>C<sub>2</sub>T<sub>x</sub>/NF electrode appears as a Pd-Ni bond that not present in the Pd/NF electrode. This indicates that with the introduction of the NiFeP-Ti<sub>3</sub>C<sub>2</sub>T<sub>x</sub> structure, Pd interacts with NiFeP-Ti<sub>3</sub>C<sub>2</sub>T<sub>x</sub>, leading to a significant change in the coordination environment of Pd. The newly formed Pd-Ni bond replaces the original part of the Pd-Pd and Pd-O

bonds. The formation of the Pd-Ni bond, a new coordination environment, favors the transfer of electrons between the Pd and Ni elements. This corresponds to the previously found XPS analysis results of the Pd/NiFeP-Ti<sub>3</sub>C<sub>2</sub>T<sub>x</sub>/NF electrode with a decrease in the charge of the Ni element and an increase in the charge of the Pd element, suggesting that there is an electron transfer between the Pd and Ni elements.

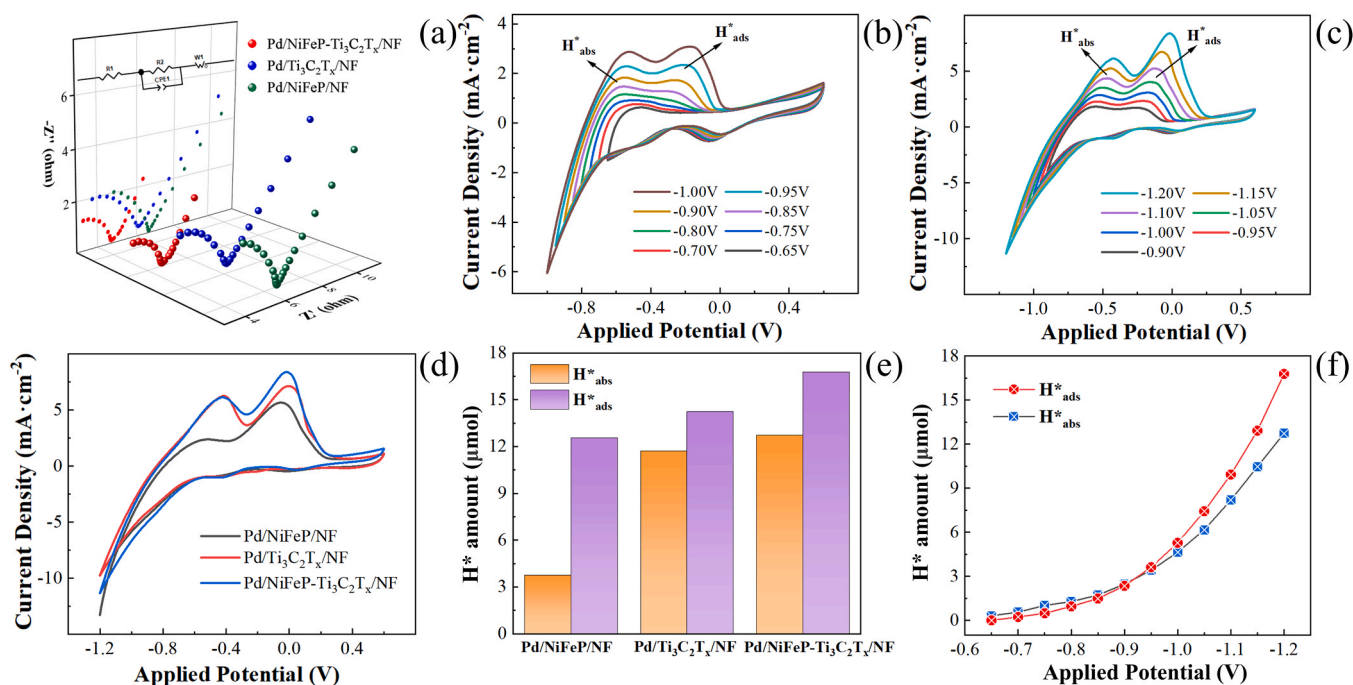


**Fig. 3.** (a) EIS of Pd/NiFeP/NF, Pd/Ti<sub>3</sub>C<sub>2</sub>T<sub>x</sub>/NF, and Pd/NiFeP-Ti<sub>3</sub>C<sub>2</sub>T<sub>x</sub>/NF electrodes, CV curves of Pd/NiFeP-Ti<sub>3</sub>C<sub>2</sub>T<sub>x</sub>/NF electrode in  $0.1 \text{ mol L}^{-1} \text{ Na}_2\text{SO}_4$  at different starting potentials (b)  $-0.65$  to  $-1.00 \text{ V}$ , (c)  $-0.90$  to  $-1.20 \text{ V}$ , (d) CV curves of Pd/NiFeP-Ti<sub>3</sub>C<sub>2</sub>T<sub>x</sub>/NF electrode, (e) H\* amounts of Pd/NiFeP/NF, Pd/Ti<sub>3</sub>C<sub>2</sub>T<sub>x</sub>/NF, and Pd/NiFeP-Ti<sub>3</sub>C<sub>2</sub>T<sub>x</sub>/NF electrodes, (f) The amounts of H\*<sub>ads</sub> and H\*<sub>abs</sub> at Pd/NiFeP-Ti<sub>3</sub>C<sub>2</sub>T<sub>x</sub>/NF electrode under different applied potential.



### 3.3. Excellent conductivity and H<sup>+</sup> generation ability of the Pd/NiFeP-Ti<sub>3</sub>C<sub>2</sub>T<sub>x</sub>/NF electrodes

Electrochemical impedance spectroscopy (EIS) was used to evaluate the electron transfer capability of the electrodes (Fig. 3a). The analytical procedure is described in Text S9. The results demonstrate that the Pd/NiFeP-Ti<sub>3</sub>C<sub>2</sub>T<sub>x</sub>/NF electrode has a stronger conductivity favoring the electron transfer.

Cyclic voltammetry (CV) was used to study the evolution of H<sup>+</sup> at the Pd/NiFeP-Ti<sub>3</sub>C<sub>2</sub>T<sub>x</sub>/NF electrode. The two oxidation peaks in the forward scan located in the potential ranges of -0.7 V to -0.5 V and -0.4 V to -0.00 V correspond to the absorbed H<sup>+</sup> (H<sup>+</sup><sub>abs</sub>) and adsorbed H<sup>+</sup> (H<sup>+</sup><sub>ads</sub>), respectively (Fig. 3b-c) [24,25]. Clearly, the area of the two oxidation peaks gradually increases when a more negative potential is applied, proving that H<sup>+</sup> production has increased. Electrochemically active surface area (ECSA) is an important method of characterizing the number of active sites of the catalysts. The ECSA of the three electrodes are calculated and compared (Text S10) [26]. The ECSA of Pd/NiFeP-Ti<sub>3</sub>C<sub>2</sub>T<sub>x</sub>/NF (2.12 cm<sup>2</sup>) electrode is larger than that of Pd/NiFeP/NF

(1.48 cm<sup>2</sup>) and Pd/Ti<sub>3</sub>C<sub>2</sub>T<sub>x</sub>/NF (1.88 cm<sup>2</sup>) (Fig. 3d). This demonstrates vertically interleaved array NiFeP-Ti<sub>3</sub>C<sub>2</sub>T<sub>x</sub> exposes more substrate planes and edge positions, which add active sites for the electrode reaction. From the linear scanning voltammetry (LSV) of the electrodes, it can be seen that the hydrogen-evolution overpotentials of the electrodes decreased from -1.06 V to -0.41 V, which proves that the introduction of NiFeP-Ti<sub>3</sub>C<sub>2</sub>T<sub>x</sub> significantly improved the electrode's ability to generate H<sup>+</sup> (Figure S14).

Next, the amounts of H<sup>+</sup> species at the electrodes are evaluated by oxidizing charge. The amounts of H<sup>+</sup><sub>abs</sub> and H<sup>+</sup><sub>ads</sub> generated at the Pd/NiFeP-Ti<sub>3</sub>C<sub>2</sub>T<sub>x</sub>/NF electrode are the highest under the same condition, and the amounts of H<sup>+</sup><sub>abs</sub> and H<sup>+</sup><sub>ads</sub> raise with increasing potential (Fig. 3e-f). After the potential exceeds -0.95 V, the amounts of H<sup>+</sup><sub>ads</sub> are gradually higher than that of H<sup>+</sup><sub>abs</sub>, which suggests a continuous evolution among H<sup>+</sup> species as the potential increases. This may be attributed to the synergistic effect of electron-rich Pd and electron-deficient Ni in the storage and conversion of H<sup>+</sup> species.

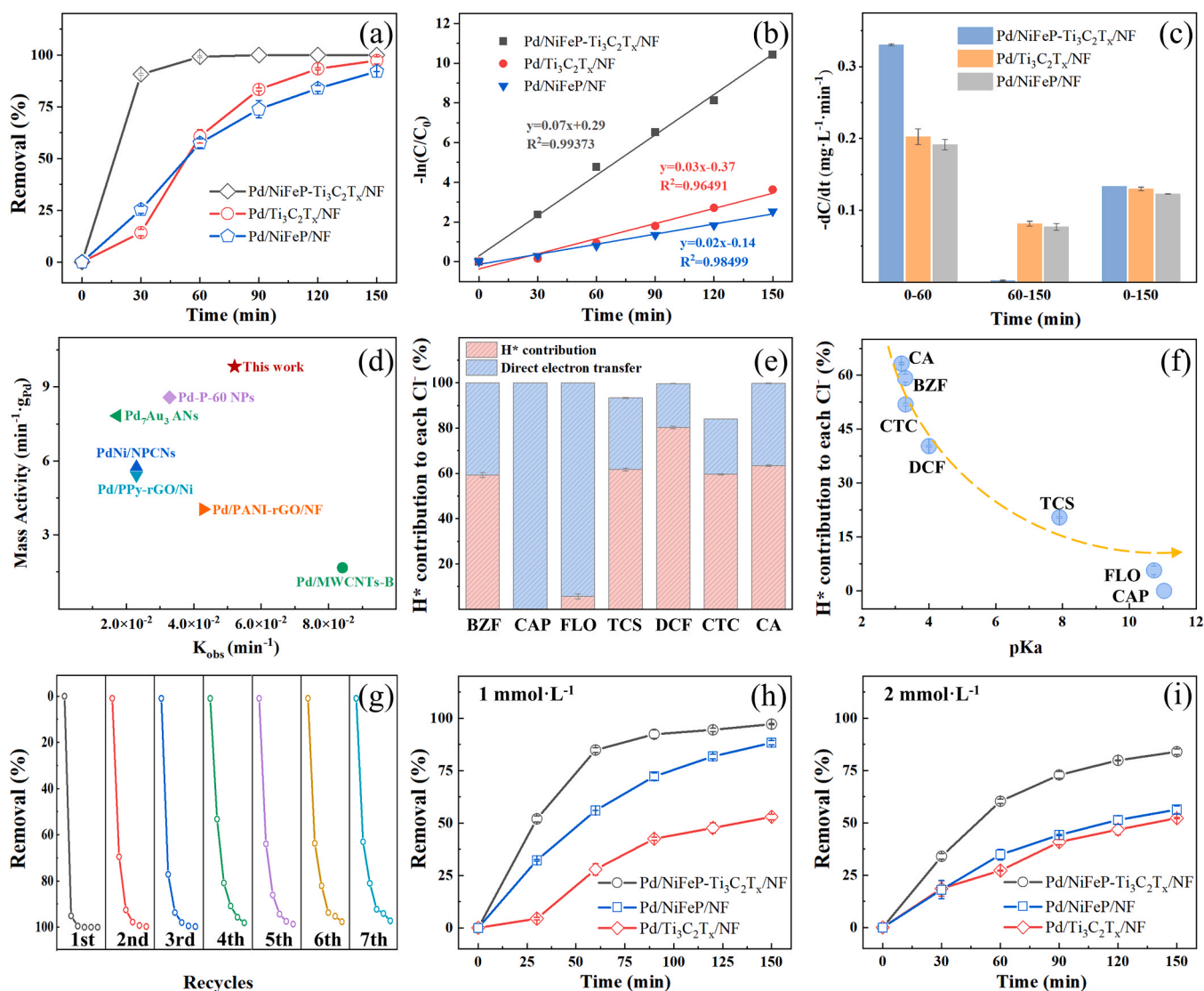


**Fig. 4.** EHDC of BZf by Pd/NiFeP-Ti<sub>3</sub>C<sub>2</sub>T<sub>x</sub>/NF, Pd/NiFeP/NF, and Pd/Ti<sub>3</sub>C<sub>2</sub>T<sub>x</sub>/NF electrodes (a) EHDC removal efficiency, (b) Reaction kinetics, (c) Removal rate of BZf at different times, (d) Dechlorination ability of Pd/NiFeP-Ti<sub>3</sub>C<sub>2</sub>T<sub>x</sub>/NF electrode for 4-CP in comparison with the existing literatures, (e) Contribution of indirect and direct electron transfer to EHDC, (f) Plot of relationship between pKa and H<sup>+</sup> contribution to Cl<sup>-</sup> for different chlorinated PPCPs, (g) Stability test of Pd/NiFeP-Ti<sub>3</sub>C<sub>2</sub>T<sub>x</sub>/NF electrode, the dichlorination performance of three electrodes for BZf at different SO<sub>3</sub><sup>2-</sup> concentrations (h) 1 mmol·L<sup>-1</sup>, (i) 2 mmol·L<sup>-1</sup> (experimental condition: temperature = 40°C, current densities = 1.75 mA·cm<sup>-2</sup>, concentration of pollutants = 20 mg·L<sup>-1</sup>).

### 3.4. Electrocatalytic dechlorination experiments demonstrating the excellent dechlorination ability of the Pd/NiFeP-Ti<sub>3</sub>C<sub>2</sub>T<sub>x</sub>/NF electrode

The EHDC performances of three electrodes for the removal of bezafibrate (BZF) were explored. Obviously, the Pd/NiFeP-Ti<sub>3</sub>C<sub>2</sub>T<sub>x</sub>/NF electrode is more effective and can completely remove BZF after 90 min of reaction time. Under the same conditions, the Pd/NiFeP/NF and Pd/Ti<sub>3</sub>C<sub>2</sub>T<sub>x</sub>/NF electrodes remove only 73.86% and 83.4% at 90 min, and only 92.04% and 97.35% at 150 min, respectively (Fig. 4a). After fitting, it is found that the EHDC processes on the electrodes follow pseudo first-order kinetics (Fig. 4b). Pd/NiFeP-Ti<sub>3</sub>C<sub>2</sub>T<sub>x</sub>/NF electrode has a maximum EHDC reaction rate constant ( $k_{\text{obs}}$ ) of 0.07 min<sup>-1</sup> for BZF, which is 3.5 and 2.3 times higher than that of Pd/NiFeP/NF (0.02 min<sup>-1</sup>) and Pd/Ti<sub>3</sub>C<sub>2</sub>T<sub>x</sub>/NF (0.03 min<sup>-1</sup>), respectively. The results show that the Pd/NiFeP-Ti<sub>3</sub>C<sub>2</sub>T<sub>x</sub>/NF electrode has better EHDC performance under the same operating conditions. The catalytic performance of the electrode is not only determined by the final removal efficiency, but the removal rate is also an important factor [27]. The removal rates of BZF at the Pd/NiFeP-Ti<sub>3</sub>C<sub>2</sub>T<sub>x</sub>/NF, Pd/Ti<sub>3</sub>C<sub>2</sub>T<sub>x</sub>/NF, and Pd/NiFeP/NF electrodes are 0.331, 0.202, and 0.191 mg·L<sup>-1</sup>·min<sup>-1</sup> averaged over 60 min, respectively (Fig. 4c). The Pd/NiFeP-Ti<sub>3</sub>C<sub>2</sub>T<sub>x</sub>/NF electrode possesses the fastest removal rate of BZF, indicating it has the best electrocatalytic activity. Meanwhile, the effects of different temperatures and current densities on the dechlorination performance of the Pd/NiFeP-Ti<sub>3</sub>C<sub>2</sub>T<sub>x</sub>/NF electrode are explored (Figure S15). The suitable temperature and current density can favor the EHDC process. It is worth noting that the dechlorination efficiencies of the electrodes are greatly reduced in the absence of the Pd, which proves the importance of Pd in the EHDC process (Text S11 and Figure S16).

To elucidate the entire dechlorination pathway of BZF removal by the Pd/NiFeP-Ti<sub>3</sub>C<sub>2</sub>T<sub>x</sub>/NF electrode, ultra-performance liquid chromatography-mass spectrometry (UPLC-MS) analysis was performed to detect the reduction products of BZF during the EHDC reaction. The toxicities of BZF and the dechlorination product are also analyzed. The details of analyzing the dechlorination reaction pathway and toxicity are studied in Text S12. The toxicity of BZF in the ecosystem is significantly reduced by the EHDC process, which will provide a simple, efficient and green solution for the treatment of difficult-to-remove chlorinated pollutants in the future.

To explore the general applicability of electrodes for chlorinated PPCPs, six additional PPCPs, namely chloramphenicol (CAP), florfenicol (FLO), triclosan (TCS), diclofenac sodium (DCF), chlortetracycline (CTC), and clofibric acid (CA) are selected as the target pollutants to further validate the EHDC performance of the Pd/NiFeP-Ti<sub>3</sub>C<sub>2</sub>T<sub>x</sub>/NF electrode. We found that the electrode has a very high removal efficiency for all types of chlorinated PPCPs. The detailed inquiry process is discussed in Text S13.

Since there are relatively few studies on emerging chlorinated PPCPs in the field of EHDC, 4-chlorophenol (4-CP) is chosen as a pollutant for the dechlorination experiments to cross-check the dechlorination ability of the Pd/NiFeP-Ti<sub>3</sub>C<sub>2</sub>T<sub>x</sub>/NF electrode. The Pd/NiFeP-Ti<sub>3</sub>C<sub>2</sub>T<sub>x</sub>/NF electrode removes 99.8% of 4-CP at a concentration of 0.5 mmol·L<sup>-1</sup> in 120 min, with  $k_{\text{obs}}$  of 0.0521 min<sup>-1</sup> (Figure S25). The dechlorination performance of Pd/NiFeP-Ti<sub>3</sub>C<sub>2</sub>T<sub>x</sub>/NF electrode for 4-CP is compared with the catalysts in the literature, and the results are shown in Fig. 4d and Table S3. The mass activity (MA) is the catalytic rate or  $k_{\text{obs}}$  (expressed as the rate constant) per unit mass of Pd catalyst. The MA of the Pd/NiFeP-Ti<sub>3</sub>C<sub>2</sub>T<sub>x</sub>/NF electrode (9.83 min<sup>-1</sup>·m<sub>Pd</sub><sup>-1</sup>) is highest compared with other catalysts [28–33], which indicates that Pd/NiFeP-Ti<sub>3</sub>C<sub>2</sub>T<sub>x</sub>/NF electrode has the highest utilization for Pd (Fig. 4d and Table S3). This proves the general applicability and extremely high catalytic activity of the Pd/NiFeP-Ti<sub>3</sub>C<sub>2</sub>T<sub>x</sub>/NF electrode for removing chlorinated pollutants. Meanwhile, The EHDC process can effectively remove difficult-to-degrade chlorinated pollutants with very low  $E_{\text{EO}}$  of 0.192, 0.402, and 0.258 kWh/m<sup>3</sup>/order for BZF, DCF, and 4-CP, respectively (i.e., a figure of merit represents the electrical energy

needed to reduce the amounts of pollutants by one order of magnitude within a unit volume; Text S14 and Table S4 for details). The  $E_{\text{EO}}$  values are several orders of magnitude lower than other water treatment technologies such as TiO<sub>2</sub>/Ti film vacuum ultraviolet (VUV) catalysis (53.08 kWh/m<sup>3</sup>/order for BZF) [34], GO/TiO<sub>2</sub> photocatalytic membrane (14 kWh/m<sup>3</sup>/order for DCF) [35], CuFe<sub>2</sub>O<sub>4</sub> electrochemical activation of peroxymonosulfate (2.12 kWh/m<sup>3</sup>/order for DCF) [36], and Fe/N/S-TiO<sub>2</sub> visible-light photocatalysis (14.5 kWh/m<sup>3</sup>/order for 4-CP) [37].

### 3.5. H<sup>•</sup> plays a crucial role in the dechlorination process of electrodes

To demonstrate the role played by H<sup>•</sup> in the EHDC process, the direct or indirect reduction mechanism of the Pd/NiFeP-Ti<sub>3</sub>C<sub>2</sub>T<sub>x</sub>/NF electrode for the different chlorinated PPCPs is investigated. Tert-butanol (TBA) is a specific quencher for H<sup>•</sup> [38], is used to determine the role of H<sup>•</sup> in EHDC of chlorinated pollutants in cathodic systems. The inhibitory effect of the Pd/NiFeP-Ti<sub>3</sub>C<sub>2</sub>T<sub>x</sub>/NF electrode on the removal of BZF increases significantly with the TBA concentration increases from 0.2 to 1.0 mol·L<sup>-1</sup> (Figure S26). Ultimately, 1 mol·L<sup>-1</sup> of TBA is able to determine the complete quenching of H<sup>•</sup>. The removal efficiency of Pd/NiFeP-Ti<sub>3</sub>C<sub>2</sub>T<sub>x</sub>/NF electrode for BZF is 40.77% when the concentration of TBA is 1.0 mol·L<sup>-1</sup>. The contribution of H<sup>•</sup> to BZF removal is seen to account for 59.23%, which indicates that the EHDC reaction of Pd/NiFeP-Ti<sub>3</sub>C<sub>2</sub>T<sub>x</sub>/NF electrode for BZF is leading by indirect dechlorination dominated by H<sup>•</sup> (H<sup>•</sup> contribution). Additionally, the mechanism of direct or indirect reductive dechlorination of other chlorinated PPCPs by Pd/NiFeP-Ti<sub>3</sub>C<sub>2</sub>T<sub>x</sub>/NF electrode is investigated (Fig. 4e and Figure S27). For CAP and FLO, it is observed that the removal of both pollutants is essentially uninhibited at the TBA concentration of 1.0 mol·L<sup>-1</sup>. The removal efficiency of CAP is still 100% at 150 min, and the removal efficiency of FLO can reach 94.31%, which proves that the removal of CAP and FLO by Pd/NiFeP-Ti<sub>3</sub>C<sub>2</sub>T<sub>x</sub>/NF is a direct reduction process. Inhibition of TCS, DCF, and CTC removal by Pd/NiFeP-Ti<sub>3</sub>C<sub>2</sub>T<sub>x</sub>/NF electrode is significantly enhanced under the TBA concentration of 1.0 mol·L<sup>-1</sup>. The removal efficiencies of the TCS, DCF, and CTC could only reach 38.34%, 67.60%, and 40.41%, respectively. The contributions of H<sup>•</sup> to the removal of TCS, DCF and CTC are 58.91%, 32.13%, and 43.9%, respectively, indicating that the EHDC reactions of TCS, DCF, and CTC at the Pd/NiFeP-Ti<sub>3</sub>C<sub>2</sub>T<sub>x</sub>/NF electrode are mainly indirect dechlorination dominated by H<sup>•</sup>. For CA, the removal efficiency rapidly decreases to 36.82% when TBA is added, again demonstrating that the contribution of H<sup>•</sup> dominates the system.

Interestingly, the relationship between H<sup>•</sup> contribution to each Cl<sup>-</sup> and pollutant structure is found by comparing the data (Table S5). The smaller the acidity coefficient (pKa), the easier it is for pollutants to be removed by indirect reductive dechlorination with H<sup>•</sup> contribution (Fig. 4f). The higher the proportion of pollutants removed by indirect dechlorination (via H<sup>•</sup>), the more the areas of the CV peaks are reduced by the addition of the pollutants (Figure S28 and Table S5). The possible reason for this is that for pollutants with smaller pKa, it is easier to dissociate the proton H<sup>+</sup>, which provides a greater source of H<sup>•</sup> generation. Thus, indirect reductive dechlorination reaction with H<sup>•</sup> contribution is more likely to occur during the removal of pollutants. Importantly, this is the first study to probe the relationship between free radicals of EHDC and pollutant structure, which will provide a novel strategy for the preparation of catalysts in the field of EHDC. The Pd/NiFeP-Ti<sub>3</sub>C<sub>2</sub>T<sub>x</sub>/NF electrode exhibits excellent performance whether dechlorination is carried out by indirect or direct electron transfer, this is due to its abundant H<sup>•</sup> production and excellent electrical conductivity.

### 3.6. Probing the stability and durability of the Pd/NiFeP-Ti<sub>3</sub>C<sub>2</sub>T<sub>x</sub>/NF electrodes

The reusability performance is a key indicator to evaluate the

stability of the electrodes. The durability of the Pd/NiFeP-Ti<sub>3</sub>C<sub>2</sub>T<sub>x</sub>/NF electrode is further investigated by performing seven more cycle experiments. The Pd/NiFeP-Ti<sub>3</sub>C<sub>2</sub>T<sub>x</sub>/NF electrode maintains a high efficiency of EHDC for seven cycles, and the removal efficiency of BZF by the Pd/NiFeP-Ti<sub>3</sub>C<sub>2</sub>T<sub>x</sub>/NF electrode still reaches 97.5% at the seventh cycle. Even though the dechlorination efficiency of the Pd/NiFeP-Ti<sub>3</sub>C<sub>2</sub>T<sub>x</sub>/NF electrode drops a little, it remains stable in the later stages (Fig. 4g). The changes of valences and binding energies of the Pd and Ni elements in the used electrodes changed are very little, which proved the stability of the electrodes in long-term use (Figure S29, Figure S30, Table S6 and Table S7). The results demonstrate the strong stability of the Pd/NiFeP-Ti<sub>3</sub>C<sub>2</sub>T<sub>x</sub>/NF electrode. The high durability shown by the electrode can be attributed to the formation of a stable heterojunction structure by the strong interaction between NiFeP-Ti<sub>3</sub>C<sub>2</sub>T<sub>x</sub> and Pd.

The wastewater treatment process must be a continuous process, so an excellent electrode needs to maintain high dechlorination efficiency in various harsh environments. Sulfur-containing molecules can be strongly adsorbed onto the catalyst surface and inhibit the catalytic reaction, which significantly reduces the catalytic performance [39]. Therefore, exploring the resistance of electrode to sulfur-containing species is crucial in practical applications. The effects of the sulfur-containing molecules on the EHDC of three electrodes are investigated using sulfite (SO<sub>3</sub><sup>2-</sup>) as the target substance, respectively. The specific effects of different concentrations of SO<sub>3</sub><sup>2-</sup> on the three electrodes are discussed in Text S15. The Pd/NiFeP-Ti<sub>3</sub>C<sub>2</sub>T<sub>x</sub>/NF electrode shows excellent EHDC performance compared to other electrodes in the presence of different concentrations of SO<sub>3</sub><sup>2-</sup> (Fig. 4h and i). This may be due to sulfur atoms are embedded in the NiFeP-Ti<sub>3</sub>C<sub>2</sub>T<sub>x</sub> surface during the reaction process, and the NiFeP-Ti<sub>3</sub>C<sub>2</sub>T<sub>x</sub> vertical structure provides

support for the formation of new reaction centers with higher activity, which slows down the process of electrode deactivation to a certain extent. Additionally, nickel reacts easily with sulfur to form nickel sulfide, so nickel competes with Pd, which reduces the deactivation of Pd and further slows down the sulfur poisoning [40].

It is not sufficient to evaluate the durability of the Pd/NiFeP-Ti<sub>3</sub>C<sub>2</sub>T<sub>x</sub>/NF electrode for sulfur species. For practical applications, it is also necessary to evaluate the effect of anions (Cl<sup>-</sup>, CO<sub>3</sub><sup>2-</sup>, HCO<sub>3</sub><sup>-</sup>, NO<sub>3</sub><sup>-</sup>, and NO<sub>2</sub><sup>-</sup>) typically present in the water bodies because they may poison the active sites or react with H<sup>+</sup> and increase H<sup>+</sup> consumption [41]. The detailed exploratory section is displayed in Text S16. The Pd/NiFeP-Ti<sub>3</sub>C<sub>2</sub>T<sub>x</sub>/NF electrode maintains excellent dechlorination performance in the presence of various ions, which suggests that it can be used as a catalytic electrode for practical water treatment processes.

### 3.7. Why electron-rich Pd and electron-deficient Ni are formed and how they optimize the adsorption ability of the Pd/NiFeP-Ti<sub>3</sub>C<sub>2</sub>T<sub>x</sub>/NF electrodes

To gain insight into the heterojunction effect of the Pd/NiFeP-Ti<sub>3</sub>C<sub>2</sub>T<sub>x</sub>/NF electrodes, DFT calculations are used to explore the changes in the electronic structure (Figure S32a-c). The charge density difference of the Pd/NiFeP-Ti<sub>3</sub>C<sub>2</sub>T<sub>x</sub> heterostructure confirms the charge redistribution phenomenon (Fig. 5a). The electron density of Pd atoms at the interface increases, while that of Ni and Fe atoms decreases (red regions gain electrons, yellow regions lose electrons). Meanwhile, electron localization function (ELF) analysis is performed at the interface of Pd and NiFeP-Ti<sub>3</sub>C<sub>2</sub>T<sub>x</sub> (Fig. 5b). The results show an increase in the electron density around the Pd element (red part) and a decrease in the electron

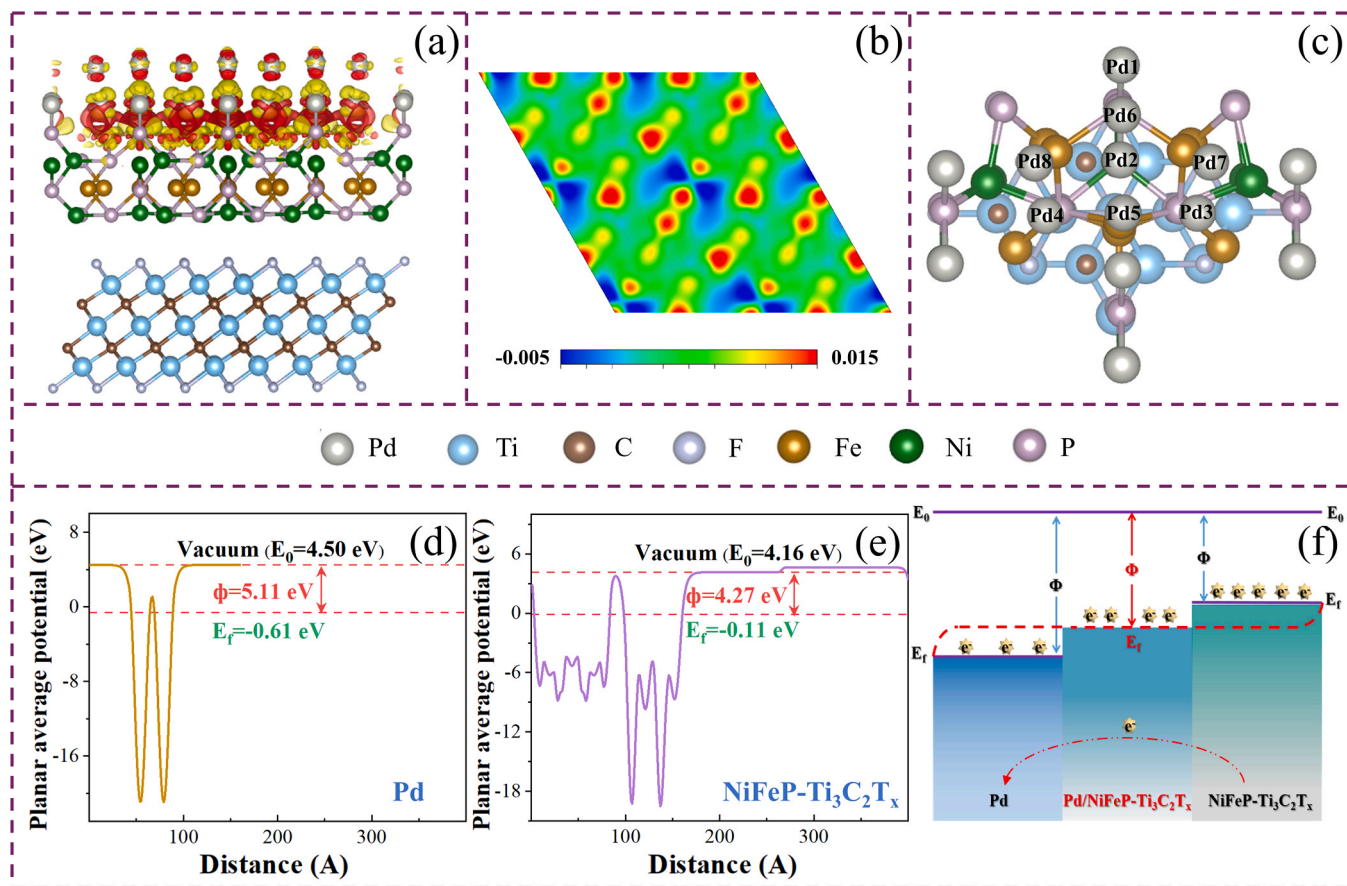


**Fig. 5.** (a) Calculated charge densities in the heterostructures of Pd/NiFeP-Ti<sub>3</sub>C<sub>2</sub>T<sub>x</sub>/NF, (b) ELF at the interface of Pd and NiFeP-Ti<sub>3</sub>C<sub>2</sub>T<sub>x</sub>, and (c) Bader analysis of Pd on the model of Pd/NiFeP-Ti<sub>3</sub>C<sub>2</sub>T<sub>x</sub>/NF heterojunction, electrostatic potential curves calculated with the figure of merit ( $E_0$ : vacuum energy level,  $\Phi$ : work function,  $E_f$ : fermi level) (d) Pd surface, (e) NiFeP-Ti<sub>3</sub>C<sub>2</sub>T<sub>x</sub> surface, (f) Schematic diagram of electron transfer between Pd and NiFeP-Ti<sub>3</sub>C<sub>2</sub>T<sub>x</sub>.



density of NiFeP-Ti<sub>3</sub>C<sub>2</sub>T<sub>x</sub> (blue part). The ELF results show the occurrence of the electron transfer phenomenon, as do the results of the electron density distribution in Fig. 5a.

To determine the specific number of electrons transferred, Bader analysis on the Pd/NiFeP-Ti<sub>3</sub>C<sub>2</sub>T<sub>x</sub>/NF electrode is performed. The number of electrons lost or gained by an element is equal to the difference between the Bader value and the valence electrons. The results show that both Pd atoms gain electrons, while both Ni and Fe atoms lost electrons (Fig. 5c and Table S8). In conclusion, after the formation of the Pd/NiFeP-Ti<sub>3</sub>C<sub>2</sub>T<sub>x</sub> heterojunction, a directional electron transfer occurs, resulting in the formation of electron-rich Pd and electron-deficient Ni. This corresponds to the results of the previous XPS analyses. The crucial role of electron-rich Pd in the field of EHDC has been demonstrated by many literatures [1,28]. As mentioned earlier, the electron-deficient Ni is able to greatly increase the capacity of water splitting of the catalyst due to  $e_g$  orbital occupancy [22,23]. It is therefore speculated that the formation of electron-rich Pd and electron-deficient Ni is likely to be the reason for the excellent dechlorination performance of the Pd/NiFeP-Ti<sub>3</sub>C<sub>2</sub>T<sub>x</sub>/NF electrode.

To explore the detailed reasons for the formation of electron-rich Pd, the work functions of Pd and NiFeP-Ti<sub>3</sub>C<sub>2</sub>T<sub>x</sub> are further calculated. The work function represents the energy barrier that prevents electrons in the fermi level ( $E_f$ ) from escaping the solid, which is equal to the energy difference between the vacuum level ( $E_0$ ) and the  $E_f$ . When two different materials interact, electrons tend to transfer from the side with the higher  $E_f$  to the side with the lower  $E_f$  until the two  $E_f$  levels reach unity [42]. As shown in Fig. 5d-e, the calculated work function of Pd (5.11 eV) is higher than that of NiFeP-Ti<sub>3</sub>C<sub>2</sub>T<sub>x</sub> (4.27 eV), reflecting the lower  $E_f$  of Pd (-0.61 eV) than that of NiFeP-Ti<sub>3</sub>C<sub>2</sub>T<sub>x</sub> (-0.11 eV). With the formation of Pd/NiFeP-Ti<sub>3</sub>C<sub>2</sub>T<sub>x</sub> heterojunction, free electrons will be transferred from NiFeP-Ti<sub>3</sub>C<sub>2</sub>T<sub>x</sub> to Pd until the  $E_f$  reach equilibrium (Fig. 5f) [43]. This is consistent with the previous analyses of XPS and charge density. This explains why the electrons of the Ni and Fe elements in the NiFeP-Ti<sub>3</sub>C<sub>2</sub>T<sub>x</sub> structure are spontaneously transferred to Pd, resulting in the formation of electron-rich Pd and electron-deficient Ni. For electron-rich Pd, Pd/NiFeP-Ti<sub>3</sub>C<sub>2</sub>T<sub>x</sub>/NF is expected to show optimized

adsorption of EHDC intermediates and display higher catalytic activity. Figure S33a-c show that the d-band centers ( $\epsilon_d$ ) of Pd/Ti<sub>3</sub>C<sub>2</sub>T<sub>x</sub>, Pd/NiFeP, and optimized Pd/NiFeP-Ti<sub>3</sub>C<sub>2</sub>T<sub>x</sub> heterostructure models are -1.45 eV, -1.32 eV, and -1.26 eV, respectively. The closer the  $\epsilon_d$  is to 0 eV, the stronger the adsorption energy is [44]. The Pd/NiFeP-Ti<sub>3</sub>C<sub>2</sub>T<sub>x</sub> heterostructure has the strongest adsorption capacity, which suggests that NiFeP-Ti<sub>3</sub>C<sub>2</sub>T<sub>x</sub> enhances the binding of Pd to H<sup>+</sup> and pollutants compared to Ti<sub>3</sub>C<sub>2</sub>T<sub>x</sub> or NiFeP alone. Since the removal of pollutants occurs on the catalyst surface, the enhanced adsorption capacity facilitates the dechlorination reaction, which is why Pd/NiFeP-Ti<sub>3</sub>C<sub>2</sub>T<sub>x</sub>/NF can have the best dechlorination performance.

### 3.8. Electron-rich Pd and electron-deficient Ni confer a lower water splitting energy barrier to the Pd/NiFeP-Ti<sub>3</sub>C<sub>2</sub>T<sub>x</sub>/NF electrodes

After demonstrating the modulation mechanism of the adsorption energy of the Pd/NiFeP-Ti<sub>3</sub>C<sub>2</sub>T<sub>x</sub>/NF electrode, it is further explored how the electron-rich Pd and electron-deficient Ni promote the water splitting of the electrode. An energy step diagram of the water splitting process is constructed for the three electrodes, starting with the adsorption of water molecules ( $H_2O^*$ ) at the electrode, followed by the breakage of the H-O bond of the  $H_2O$  molecules (activation of  $H_2O$ ) to produce adsorbed (H-OH)<sup>\*</sup>, and ending with the desorption of -OH to leave only the adsorbed H<sup>+</sup> ( $H^*+OH$ ) (Fig. 6a-c). All three electrodes tended to produce adsorbed H<sup>+</sup> rather than adsorbed OH<sup>\*</sup> (lower energy barriers) after activation of  $H_2O$ , which is speculated to result from the excellent catalytic effect of Pd in the EHDC process (Figure S34). Importantly, it has been documented that activation of  $H_2O$  is the rate-determining step (RDS) in the water splitting process, and it has a critical influence on the overall reaction [45,46]. It can be seen that the RDS energy barrier of Pd/NiFeP-Ti<sub>3</sub>C<sub>2</sub>T<sub>x</sub>/NF (0.063 eV) during H<sup>+</sup> generation is reduced by 92.38% and 80.06% compared to Pd/NiFeP/NF (0.827 eV) and Pd/Ti<sub>3</sub>C<sub>2</sub>T<sub>x</sub>/NF (0.316 eV), respectively (Fig. 6d). The lower energy barrier of RDS will favor the reaction, so Pd/NiFeP-Ti<sub>3</sub>C<sub>2</sub>T<sub>x</sub>/NF can produce more H<sup>+</sup> for EHDC.

Because the process of EHDC of pollutants by H<sup>+</sup> occurs on the

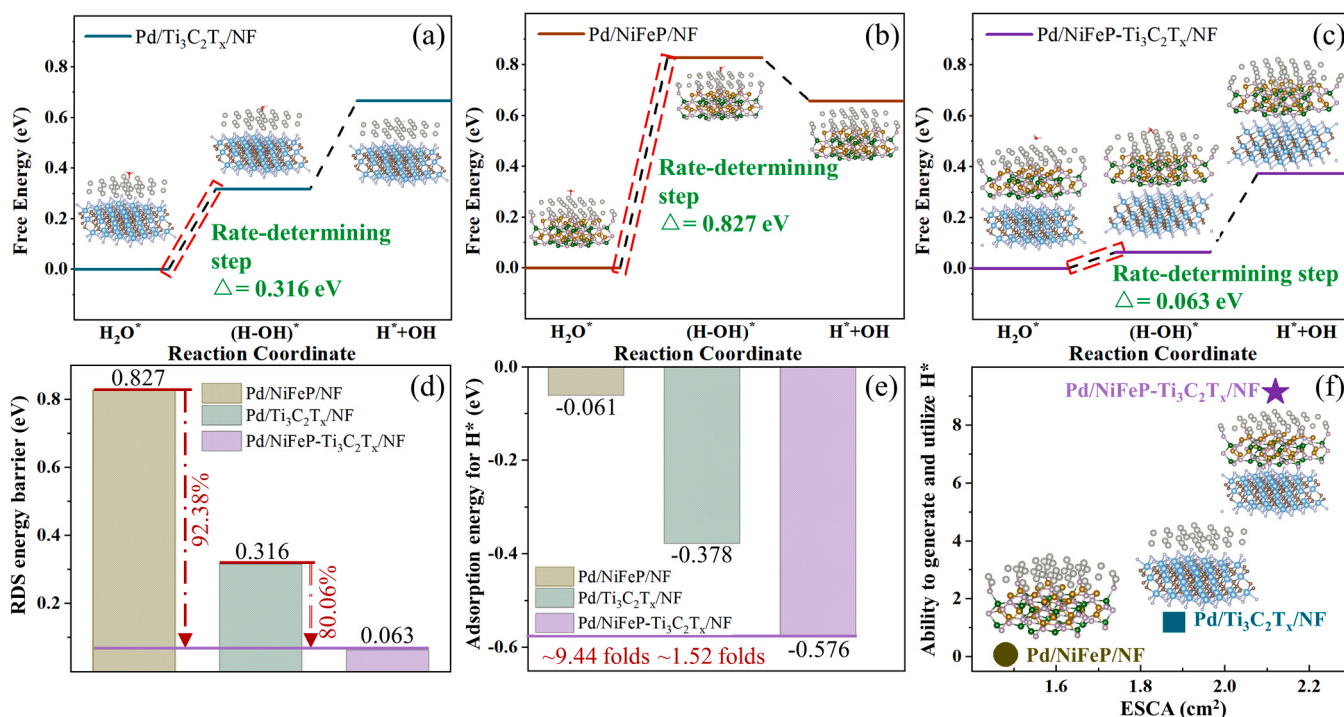


Fig. 6. Free energy step diagrams of H<sup>+</sup> generation of (a) Pd/Ti<sub>3</sub>C<sub>2</sub>T<sub>x</sub>/NF, (b) Pd/NiFeP/NF, (c) Pd/NiFeP-Ti<sub>3</sub>C<sub>2</sub>T<sub>x</sub>/NF, Comparison of (d) RDS energy barrier, and (e) H<sup>+</sup> adsorption energy of three electrodes, (f) ECSA of three electrodes and the ability to generate and utilize H<sup>+</sup>.

catalyst surface, a catalyst with excellent dechlorination performance should have a strong adsorption ability for  $H^*$  [47]. The adsorption energies of the three electrodes for  $H^*$  ( $E_{ads}(H^*)$ ) are calculated (Figure S35). The adsorption energy of Pd/NiFeP-Ti<sub>3</sub>C<sub>2</sub>T<sub>x</sub>/NF (-0.576 eV) for  $H^*$  is roughly 9.44 and 1.52 folds stronger than that of Pd/NiFeP/NF (-0.061 eV) and Pd/Ti<sub>3</sub>C<sub>2</sub>T<sub>x</sub>/NF (-0.378 eV), respectively (Fig. 6e). The Pd/NiFeP-Ti<sub>3</sub>C<sub>2</sub>T<sub>x</sub>/NF electrode has the strongest adsorption energy for  $H^*$ , which enables more efficient use of the generated  $H^*$ . Theoretically, the lower the RDS energy barrier produced by  $H^*$ , the easier it is for the electrode to produce  $H^*$ . At the same time, because the  $H^*$ -dominated EHDC process occurs on the surface of the electrode, the stronger the adsorption energy of the electrode for  $H^*$ , the more favorable it is for the utilization of  $H^*$ . We therefore propose to define the ability of the electrode to generate and utilize  $H^*$  in terms of the ratio of the adsorption energy of the electrode for  $H^*$  to the RDS energy barrier generated by  $H^*$  (Absolute values are used to the adsorption energy for  $H^*$ ). The higher the calculated value of the ability to generate and utilize  $H^*$ , the better the ability of the material to efficiently utilize more  $H^*$ . It can be seen that the ability of Pd/NiFeP-Ti<sub>3</sub>C<sub>2</sub>T<sub>x</sub>/NF (9.14) for  $H^*$  generation and utilization is 123.51 and 7.62 folds higher than that of Pd/NiFeP/NF (0.074) and Pd/Ti<sub>3</sub>C<sub>2</sub>T<sub>x</sub>/NF (1.20), respectively (Fig. 6f). Meanwhile, Pd/NiFeP-Ti<sub>3</sub>C<sub>2</sub>T<sub>x</sub>/NF electrode has the highest ECSA, which will greatly benefit the process of  $H^*$  dichlorination. This explains why Pd/NiFeP-Ti<sub>3</sub>C<sub>2</sub>T<sub>x</sub>/NF electrodes are able to perform excellently in EHDC processes. Although Pd and Ni are also present in Pd/NiFeP/NF, its ability to produce  $H^*$  and utilize  $H^*$  is hundreds of times worse than that of Pd/NiFeP-Ti<sub>3</sub>C<sub>2</sub>T<sub>x</sub>/NF. This suggests that the synergistic role of electron-rich Pd and electron-deficient Ni makes a crucial contribution to the EHDC process.

### 3.9. Efficient utilization of $H^*$ for pollutant removal through the synergistic role of electron-rich Pd and electron-deficient Ni

The mechanism of how electron-rich Pd and electron-deficient Ni utilize  $H^*$  for efficient removal of pollutants is studied in depth by us, this will provide researchers with more thoughts on the synergistic role between metals for environmental catalysis. The adsorption energies of electron-rich Pd and electron-deficient Ni for  $H^*$  in the Pd/NiFeP-Ti<sub>3</sub>C<sub>2</sub>T<sub>x</sub>/NF electrode are almost the same, -0.40 eV and -0.39 eV,

respectively, which suggests that both Pd and Ni can efficiently adsorb  $H^*$  on the surface for utilization. Next the migration energies of  $H^*$  for the three paths between Pd and Pd (Pd-Pd), between Ni and Ni (Ni-Ni), and between Pd, and Ni (Pd-Ni) are calculated (Fig. 7a).  $H^*$  has the lowest migration barrier for Pd-Ni (0.143 eV), which is reduced by 75.76% and 71.68% compared to Pd-Pd (0.590 eV) and Ni-Ni (0.505 eV), respectively (Fig. 7b). In order to probe the EHDC mechanism more deeply, the adsorption energies of electron-rich Pd and electron-deficient Ni for BZF in the presence of  $H^*$  are calculated. The results of Fig. 7c show that Pd (-4.216 eV) has a stronger adsorption energy for BZF than Ni (-3.263 eV). The adsorption energy of Pd for BZF increases when  $H^*$  is present. Therefore, most of the BZF are preferentially adsorbed on the Pd surface, and the  $H^*$  on the Pd surface attacks the adsorbed BZF first. Meanwhile, the adsorption sites on the Ni surface are reduced by increasing the amount of  $H^*$  on the surface, and more active sites of Pd are exposed due to the consumption of  $H^*$  on the Pd surface by BZF. Together with the extremely low migration barrier of  $H^*$  between Pd and Ni, the  $H^*$  on the Ni surface will continuously migrate to the Pd surface (Fig. 7d). Ni then serves as a source of  $H^*$  supply for Pd, and the synergistic role of Pd and Ni in attacking chlorinated pollutants by co-utilizing  $H^*$ . Meanwhile, the adsorption energy of the Pd/NiFeP-Ti<sub>3</sub>C<sub>2</sub>T<sub>x</sub>/NF for the dichlorination product is -2.765 eV, which is much weaker than the adsorption energy for the BZF (-4.216 eV). The dechlorination products can be desorbed from the electrode surface in time, thus providing more active sites for BZF removal (Figure S36 and Figure S37). This explains why the Pd/NiFeP-Ti<sub>3</sub>C<sub>2</sub>T<sub>x</sub>/NF electrode has an outstanding removal efficiency for chlorinated pollutants.

## 4. Conclusion

This study demonstrates the potential of developing an efficient chlorinated PPCPs removal technology utilizing an electrocatalytic system equipped with Pd/NiFeP-Ti<sub>3</sub>C<sub>2</sub>T<sub>x</sub>/NF electrode. The difference in the work function leads to the formation of electron-rich Pd and electron-deficient Ni, which endows the Pd/NiFeP-Ti<sub>3</sub>C<sub>2</sub>T<sub>x</sub>/NF electrode with excellent dechlorination ability. The Pd/NiFeP-Ti<sub>3</sub>C<sub>2</sub>T<sub>x</sub>/NF electrode can completely remove BZF in 90 min and maintaining a very high dechlorination efficiency (97.5%) at the seventh reuse, and it is extremely resistant to anions in natural water ( $SO_4^{2-}$ ,  $Cl^-$ ,  $CO_3^{2-}$ ,  $HCO_3^-$ ,

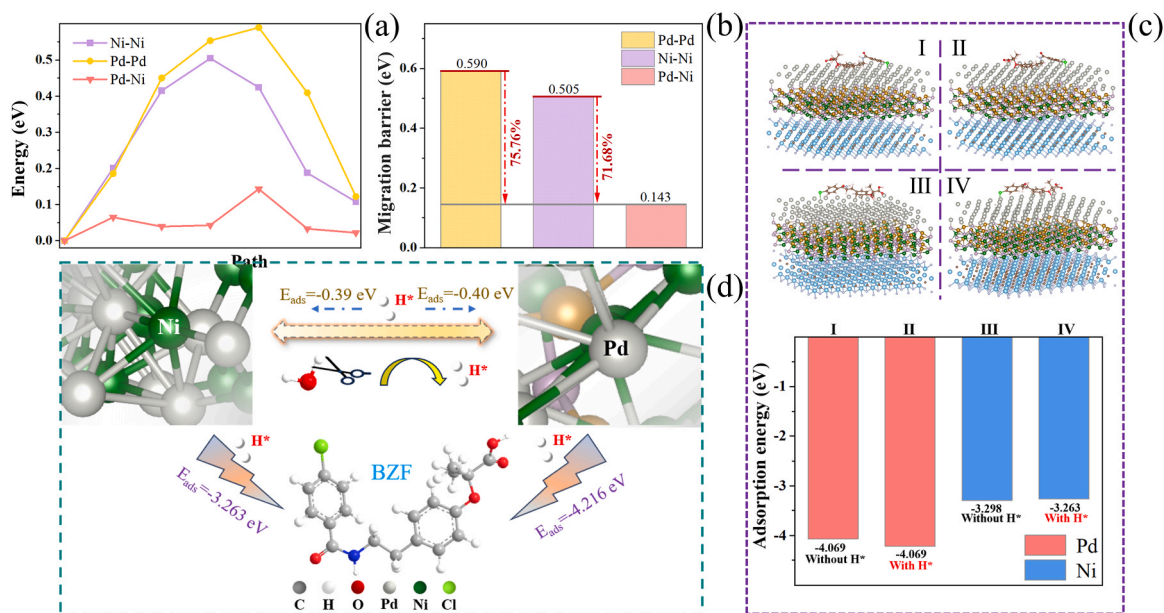


**Fig. 7.** (a) Migration energy of  $H^*$  from Pd to Pd, Ni to Ni, and Pd to Ni paths at Pd/NiFeP-Ti<sub>3</sub>C<sub>2</sub>T<sub>x</sub>/NF electrode, (b) Migration barriers of  $H^*$  from Pd to Pd, Ni to Ni, and Pd to Ni at Pd/NiFeP-Ti<sub>3</sub>C<sub>2</sub>T<sub>x</sub>/NF electrode, (c) Adsorption energies of Pd and Ni on BZF in the presence and absence of  $H^*$  at Pd/NiFeP-Ti<sub>3</sub>C<sub>2</sub>T<sub>x</sub>/NF electrode, (d) Reaction pathways of  $H^*$  with BZF at Pd/NiFeP-Ti<sub>3</sub>C<sub>2</sub>T<sub>x</sub>/NF electrode.

$\text{NO}_3^-$ , and  $\text{NO}_2^-$ ). Importantly, the relationship between the contribution of  $\text{H}^*$  to the Cl atom in chlorinated pollutants and the  $\text{pK}_a$  of the pollutants is clearly explored by us, which is the first proposal in the field of EHDC. Characterization and DFT calculations demonstrate that the synergistic role of electron-rich Pd and electron-deficient Ni dramatically reduces the energy barrier for water splitting to produce  $\text{H}^*$  (the active substance attacking the pollutant), which greatly increases the  $\text{H}^*$  production. Meanwhile, Ni can provide Pd with continuous supply of  $\text{H}^*$  to attack chlorinated pollutants due to the extremely low migration barrier between Pd and Ni. This study investigated the mechanism of electron-rich Pd and electron-deficient Ni in synergistically promoting EHDC, which will provide useful strategies for practical applications in the field of environmental catalytic remediation.

## CRediT authorship contribution statement

**Junjing Li:** Conceptualization, Methodology, Funding acquisition. **Kaizhou Kong:** Data curation, Writing – original draft, Writing – review & editing. **Shumin Ma:** Data curation. **Jing Ding:** Formal analysis. **Liang Wang:** Resources, Funding acquisition. **John Crittenden:** Supervision, Formal analysis.

## Declaration of Competing Interest

The authors declare that they have no known competing financial interests or personal relationships that could have appeared to influence the work reported in this paper.

## Data availability

Data will be made available on request.

## Acknowledgment

This work was kindly supported by National Natural Science Foundation of China (52370084), Open Project of State Key Laboratory of Urban Water Resource and Environment (QG202231), Cangzhou Institute of Tiangong University (Grant No. TGCYY-Z-0101), Hebei Natural Science Foundation (E2023110003, B2023110025). We would like to thank the Analytical & Testing Center of Tiangong University for X-ray photoelectron spectroscopy.

## Appendix A. Supporting information

Supplementary data associated with this article can be found in the online version at [doi:10.1016/j.apcatb.2024.124245](https://doi.org/10.1016/j.apcatb.2024.124245).

## References

- [1] Z. Lou, C. Yu, X. Wen, Y. Xu, J. Yu, X. Xu, Construction of Pd nanoparticles/two-dimensional Co-MOF nanosheets heterojunction for enhanced electrocatalytic hydrodechlorination, *Appl. Catal. B Environ.* 317 (2022) 121730, <https://doi.org/10.1016/j.apcatb.2022.121730>.
- [2] Z. Zheng, J. Min, X. Wang, C.W. Lung, K. Shih, I.M.C. Lo, Directional separation of highly reductive electrons to the reactive center in a magnetic S-scheme  $\text{ZnFe}_2\text{O}_4/\text{A-MoS}_2$  heterojunction for enhanced peroxymonosulfate activation toward pharmaceuticals and personal care product removal, *Environ. Sci. Technol.* 57 (2023) 8414–8425, <https://doi.org/10.1021/acs.est.2c09122>.
- [3] J. Deng, E. Gao, F. Wu, Z. You, X. Li, S. Gao, L.-Z. Huang, Generation of atomic hydrogen by Ni-Fe hydroxides: mechanism and activity for hydrodechlorination of trichloroethylene, *Water Res.* 207 (2021) 117802, <https://doi.org/10.1016/j.watres.2021.117802>.
- [4] G. Song, H. Wu, J. Jing, X. Zhang, X. Wang, S. Li, M. Zhou, Insights into electrochemical dehalogenation by non-noble metal single-atom cobalt with high efficiency and low energy consumption, *Environ. Sci. Technol.* 57 (2023) 14482–14492, <https://doi.org/10.1021/acs.est.3c06021>.
- [5] D. Huang, D.J. Kim, K. Rigby, X. Zhou, X. Wu, A. Meese, J. Niu, E. Stavitski, J.-H. Kim, Elucidating the role of single-atom Pd for electrocatalytic hydrodechlorination, *Environ. Sci. Technol.* 55 (2021) 13306–13316, <https://doi.org/10.1021/acs.est.1c04294>.
- [6] J. Li, Y. Chen, R. Bai, C. Chen, W. Wang, Y. Pan, Y. Liu, Construction of Pd/Ni<sub>2</sub>P-Ni foam nanosheet array electrode by in-situ phosphatization-electrodeposition strategy for synergistic electrocatalytic hydrodechlorination, *Chem. Eng. J.* 435 (2022) 134932, <https://doi.org/10.1016/j.cej.2022.134932>.
- [7] J. Xia, H. Zhao, B. Huang, L. Xu, M. Luo, J. Wang, F. Luo, Y. Du, C.-H. Yan, Efficient optimization of electron/oxygen pathway by constructing ceria/hydroxide interface for highly active oxygen evolution reaction, *Adv. Funct. Mater.* 30 (2020) 1908367, <https://doi.org/10.1002/adfm.201908367>.
- [8] Y. Song, B. Xu, T. Liao, J. Guo, Y. Wu, Z. Sun, Electronic structure tuning of 2D metal (hydr) oxides nanosheets for electrocatalysis, *Small* 17 (2021) 2002240, <https://doi.org/10.1002/sml.202002240>.
- [9] Y.L. Wu, X. Li, Y.S. Wei, Z. Fu, W. Wei, X.T. Wu, Q.L. Zhu, Q. Xu, Ordered macroporous superstructure of nitrogen-doped nanoporous carbon implanted with ultrafine Ru nanoclusters for efficient pH-universal hydrogen evolution reaction, *Adv. Mater.* 33 (2021) 2006965, <https://doi.org/10.1002/adma.202006965>.
- [10] J. Du, F. Li, L. Sun, Metal-organic frameworks and their derivatives as electrocatalysts for the oxygen evolution reaction, *Chem. Soc. Rev.* 50 (2021) 2663–2695, <https://doi.org/10.1039/d0cs01191f>.
- [11] L. Zhang, H. Zhao, S. Xu, Q. Liu, T. Li, Y. Luo, S. Gao, X. Shi, A.M. Asiri, X. Sun, Recent advances in 1D electrospun nanocatalysts for electrochemical water splitting, *Small Struct.* 2 (2021) 2000048, <https://doi.org/10.1002/ssr.202000048>.
- [12] J. Liu, X. Liu, H. Shi, J. Luo, L. Wang, J. Liang, S. Li, L.-M. Yang, T. Wang, Y. Huang, Q. Li, Breaking the scaling relations of oxygen evolution reaction on amorphous NiFeP nanostructures with enhanced activity for overall seawater splitting, *Appl. Catal. B: Environ.* 302 (2022) 120862, <https://doi.org/10.1016/j.apcatb.2021.120862>.
- [13] Y. Shi, M. Li, Y. Yu, B. Zhang, Recent advances in nanostructured transition metal phosphides: synthesis and energy-related applications, *Energy Environ. Sci.* 13 (2020) 4564–4582, <https://doi.org/10.1039/D0EE02577A>.
- [14] L. Wu, L. Yu, F. Zhang, B. McElhenny, D. Luo, A. Karim, S. Chen, Z. Ren, Heterogeneous bimetallic phosphide  $\text{Ni}_2\text{P-Fe}_2\text{P}$  as an efficient bifunctional catalyst for water/seawater splitting, *Adv. Funct. Mater.* 31 (2021) 2006484, <https://doi.org/10.1002/adfm.202006484>.
- [15] M. Sun, H. Liu, J. Qu, J. Li, Earth-rich transition metal phosphide for energy conversion and storage, *Adv. Energy Mater.* 6 (2016) 1600087, <https://doi.org/10.1002/aenm.201600087>.
- [16] K.R.G. Lim, A.D. Handoko, L.R. Johnson, X. Meng, M. Lin, G.S. Subramanian, B. Anasori, Y. Gogotsi, A. Vojvodic, Z.W. Seh, 2H-MoS<sub>2</sub> on Mo<sub>2</sub>CT<sub>x</sub> MXene nanohybrid for efficient and durable electrocatalytic hydrogen evolution, *ACS Nano* 14 (2020) 16140–16155, <https://doi.org/10.1021/acsnano.0c08671>.
- [17] H. Zhang, J. Diao, M. Ouyang, H. Yadegari, M. Mao, M. Wang, G. Henkelman, F. Xie, D.J. Riley, Heterostructured core-shell Ni-Co@Fe-Co nanoboxes of prussian blue analogues for efficient electrocatalytic hydrogen evolution from alkaline seawater, *ACS Catal.* 13 (2023) 1349–1358, <https://doi.org/10.1021/acscatal.2c05433>.
- [18] Z. Lv, M. Wang, D. Liu, K. Jian, R. Zhang, J. Dang, Synergetic effect of Ni<sub>2</sub>P and MXene enhances catalytic activity in the hydrogen evolution reaction, *Inorg. Chem.* 60 (2021) 1604–1611, <https://doi.org/10.1021/acs.inorgchem.0c03072>.
- [19] Y. Liao, J. Qian, G. Xie, Q. Han, W. Dang, Y. Wang, L. Lv, S. Zhao, L. Luo, W. Zhang, H.-Y. Jiang, J. Tang, 2D-layered Ti<sub>3</sub>C<sub>2</sub> MXenes for promoted synthesis of NH<sub>3</sub> on P25 photocatalysts, *Appl. Catal. B: Environ.* 273 (2020) 119054, <https://doi.org/10.1016/j.apcatb.2020.119054>.
- [20] J. Chen, Q. Long, K. Xiao, T. Ouyang, N. Li, S. Ye, Z.-Q. Liu, Vertically-interlaced NiFeP/MXene electrocatalyst with tunable electronic structure for high-efficiency oxygen evolution reaction, *Sci. Bull.* 66 (2021) 1063–1072, <https://doi.org/10.1016/j.scib.2021.02.033>.
- [21] Y. Zhao, X. Jia, G. Chen, L. Shang, G.I.N. Waterhouse, L.-Z. Wu, C.-H. Tung, D. O'Hare, T. Zhang, Ultrafine NiO nanosheets stabilized by TiO<sub>2</sub> by monolayer NiTi-LDH precursors: an active water oxidation electrocatalyst, *J. Am. Chem. Soc.* 138 (2016) 6517–6524, <https://doi.org/10.1021/jacs.6b01606>.
- [22] J. Suntivich, K.J. May, H.A. Gasteiger, J.B. Goodenough, Y. Shao-Horn, A perovskite oxide optimized for oxygen evolution catalysis from molecular orbital principles, *Science* 334 (2011) 1383–1385, <https://doi.org/10.1126/science.1212858>.
- [23] V. Viswanathan, H.A. Hansen, J. Rossmeisl, J.K. Nørskov, Universality in oxygen reduction electrocatalysis on metal surfaces, *ACS Catal.* 2 (2012) 1654–1660, <https://doi.org/10.1021/cs300227s>.
- [24] G. Jiang, M. Lan, Z. Zhang, X. Lv, Z. Lou, X. Xu, F. Dong, S. Zhang, Identification of active hydrogen species on palladium nanoparticles for an enhanced electrocatalytic hydrodechlorination of 2,4-dichlorophenol in water, *Environ. Sci. Technol.* 51 (2017) 7599–7605, <https://doi.org/10.1021/acs.est.7b01128>.
- [25] S. Qin, C. Lei, X. Wang, W. Chen, B. Huang, Electrocatalytic activation of organic chlorides via direct and indirect electron transfer using atomic vacancy control of palladium-based catalyst, *Cell. Rep. Phys. Sci.* 3 (2022) 100713, <https://doi.org/10.1016/j.xcrp.2021.100713>.
- [26] Y. Peng, M. Cui, Z. Zhang, S. Shu, X. Shi, J.T. Brosnahan, C. Liu, Y. Zhang, P. Godbold, X. Zhang, F. Dong, G. Jiang, S. Zhang, Bimetallic composition-promoted electrocatalytic hydrodechlorination reaction on silver-palladium alloy nanoparticles, *ACS Catal.* 9 (2019) 10803–10811, <https://doi.org/10.1021/acscatal.9b02282>.
- [27] J. Li, Y. Wang, B. Zhao, J. Ding, J. Zhang, M. Yin, Z. Zhang, S. Ma, Y. Liu, Z. Tan, H. Zhang, L. Wang, D.D. Dionysiou, Unraveling kinetics and mechanism of electrocatalytic hydrodechlorination of chlorinated PPCPs by nickel-cobalt metal organic framework supported palladium composite electrode, *Appl. Catal. B: Environ.* 332 (2023) 122754, <https://doi.org/10.1016/j.apcatb.2023.122754>.



- [28] Y. Chen, C. Feng, W. Wang, Z. Liu, J. Li, C. Liu, Y. Pan, Y. Liu, Electronic structure engineering of bimetallic Pd-Au alloy nanocatalysts for improving electrocatalytic hydrodechlorination performance, *Sep. Purif. Technol.* 289 (2022) 120731, <https://doi.org/10.1016/j.seppur.2022.120731>.
- [29] Y. Chen, Z. Liu, S. Liu, Y. Cheng, C. Zhang, J. Jiao, Y. Lu, W. Wang, K. Sun, X. Bi, A. Han, B. Liu, Y. Pan, Y. Liu, C. Liu, In-Situ doping-induced crystal form transition of amorphous Pd-P catalyst for robust electrocatalytic hydrodechlorination, *Appl. Catal. B: Environ.* 284 (2021) 119713, <https://doi.org/10.1016/j.apcatb.2020.119713>.
- [30] J. Li, K. Kong, Y. Chong, J. Ding, L. Wang, Z. Ba, J. Zhang, Unveiling the mechanism and performance of electrocatalytic hydrodechlorination of chlorinated PPCPs by electron-rich palladium electrode modulated through PANI-rGO interlayer, *Sep. Purif. Technol.* 323 (2023) 124452, <https://doi.org/10.1016/j.seppur.2023.124452>.
- [31] Z. Mao, L. Liu, H.B. Yang, Y. Zhang, Z. Yao, H. Wu, Y. Huang, Y. Xu, B. Liu, Atomically dispersed Pd electrocatalyst for efficient aqueous phase dechlorination reaction, *Electrochim. Acta* 391 (2021) 138886, <https://doi.org/10.1016/j.electacta.2021.138886>.
- [32] H. Yu, S. Yang, B. Zhao, Y. Lu, S. Zhu, X. Wang, W. Qin, M. Huo, Enhanced electrochemical dechlorination of 4-chlorophenol on a nickel foam electrode modified with palladium, polypyrrole and graphene, *J. Electroanal. Chem.* 869 (2020) 114099, <https://doi.org/10.1016/j.jelechem.2020.114099>.
- [33] X. Shu, Q. Yang, F. Yao, Y. Zhong, W. Ren, F. Chen, J. Sun, Y. Ma, Z. Fu, D. Wang, X. Li, Electrocatalytic hydrodechlorination of 4-chlorophenol on Pd supported multi-walled carbon nanotubes particle electrodes, *Chem. Eng. J.* 358 (2019) 903–911, <https://doi.org/10.1016/j.cej.2018.10.095>.
- [34] M. Sayed, P. Fu, L.A. Shah, H.M. Khan, J. Nisar, M. Ismail, P. Zhang, VUV-photocatalytic degradation of bezafibrate by hydrothermally synthesized enhanced {001} facets TiO<sub>2</sub>/Ti film, *J. Phys. Chem. A* 120 (2016) 118–127, <https://doi.org/10.1021/acs.jpca.5b10502>.
- [35] C. Li, Z. Lu, X. Ao, W. Sun, X. Huang, Degradation kinetics and removal efficiencies of pharmaceuticals by photocatalytic ceramic membranes using ultraviolet light-emitting diodes, *Chem. Eng. J.* 427 (2022) 130828, <https://doi.org/10.1016/j.cej.2021.130828>.
- [36] P. Xu, S. Xie, X. Liu, L. Wang, X. Jia, C. Yang, Electrochemical enhanced heterogenous activation of peroxymonosulfate using CuFe<sub>2</sub>O<sub>4</sub> particle electrodes for the degradation of diclofenac, *Chem. Eng. J.* 446 (2022) 136941, <https://doi.org/10.1016/j.cej.2022.136941>.
- [37] F.J.A. Villaluz, M.D.G. de Luna, J.I. Colades, S. Garcia-Segura, M.-C. Lu, Removal of 4-chlorophenol by visible-light photocatalysis using ammonium iron(II) sulfate-doped nano-titania, *Process Saf. Environ.* 125 (2019) 121–128, <https://doi.org/10.1016/j.psep.2019.03.001>.
- [38] J. Xu, X. Fu, Y. Liu, Y. Zhang, S. Chen, D. Li, C. Zhang, J. Gao, Y. Fu, Electrocatalytic dechlorination of florfenicol using a Pd-loaded on blue TiO<sub>2</sub> nanotube arrays cathode, *Sep. Purif. Technol.* 323 (2023) 124460, <https://doi.org/10.1016/j.seppur.2023.124460>.
- [39] G. Celik, S.A. Ailawar, S. Gunduz, J.T. Miller, P.L. Edmiston, U.S. Ozkan, Aqueous-phase hydrodechlorination of trichloroethylene over Pd-based swellable organically modified silica: catalyst deactivation due to sulfur species, *Ind. Eng. Chem. Res.* 58 (2019) 4054–4064, <https://doi.org/10.1021/acs.iecr.8b05979>.
- [40] G.I. Danmaliki, T.A. Saleh, A.A. Shamsuddeen, Response surface methodology optimization of adsorptive desulfurization on nickel/activated carbon, *Chem. Eng. J.* 313 (2017) 993–1003, <https://doi.org/10.1016/j.cej.2016.10.141>.
- [41] S. Yuan, M. Chen, X. Mao, A.N. Alshawabkeh, Effects of reduced sulfur compounds on Pd-catalytic hydrodechlorination of trichloroethylene in groundwater by cathodic H<sub>2</sub> under electrochemically induced oxidizing conditions, *Environ. Sci. Technol.* 47 (2013) 10502–10509, <https://doi.org/10.1021/es402169d>.
- [42] A. Kahn, Fermi level, work function and vacuum level, *Mater. Horiz.* 3 (2016) 7–10, <https://doi.org/10.1039/C5MH00160A>.
- [43] M. Wang, J. Duan, X. Yang, Y. Wang, Y. Duan, Q. Tang, Interfacial electric field enhanced charge density for robust triboelectric nanogenerators by tailoring metal/perovskite Schottky junction, *Nano Energy* 73 (2020) 104747, <https://doi.org/10.1016/j.nanoen.2020.104747>.
- [44] F. Ando, T. Gunji, T. Tanabe, I. Fukano, H.D. Abruña, J. Wu, T. Ohsaka, F. Matsumoto, Enhancement of the oxygen reduction reaction activity of Pt by tuning its d-band center via transition metal oxide support interactions, *ACS Catal.* 11 (2021) 9317–9332, <https://doi.org/10.1021/acscatal.1c01868>.
- [45] L. Zhang, J. Ye, Y. Tu, Q. Wang, H. Pan, L. Wu, X. Zheng, J. Zhu, Oxygen modified CoP<sub>2</sub> supported palladium nanoparticles as highly efficient catalyst for hydrolysis of ammonia borane, *Nano Res.* 15 (2022) 3034–3041, <https://doi.org/10.1007/s12274-021-3941-7>.
- [46] Q. Wang, F. Fu, S. Yang, M. Martinez Moro, M.I.A. Ramirez, S. Moya, L. Salmon, J. Ruiz, D. Astruc, Dramatic synergy in CoPt nanocatalysts stabilized by “click” dendrimers for evolution of hydrogen from hydrolysis of ammonia borane, *ACS Catal.* 9 (2019) 1110–1119, <https://doi.org/10.1021/acscatal.8b04498>.
- [47] W. Yu, H. Jiang, J. Fang, S. Song, Designing an electron-deficient Pd/NiCo<sub>2</sub>O<sub>4</sub> bifunctional electrocatalyst with an enhanced hydrodechlorination activity to reduce the consumption of Pd, *Environ. Sci. Technol.* 55 (2021) 10087–10096, <https://doi.org/10.1021/acs.est.1c01922>.